Journal of Alloys and Compounds 627 (2015) 393–401

Contents lists available at ScienceDirect

Journal of Alloys and Compounds

journal homepage: www.elsevier.com/locate/jalcom

$Co_{100-x}Fe_x$ magnetic thick films prepared by electrodeposition

M. del C. Aguirre [a,*], E. Farías [b], J. Abraham [c], S.E. Urreta [c]

[a] Instituto de Física Enrique Gaviola-Conicet-Facultad de Matemática, Astronomía y Física, Universidad Nacional de Córdoba, Ciudad Universitaria, 5000 Córdoba, Argentina
[b] Facultad de Ciencias Químicas, Universidad Nacional de Córdoba, Ciudad Universitaria, 5000 Córdoba, Argentina
[c] Facultad de Matemática, Astronomía y Física, Universidad Nacional de Córdoba, Ciudad Universitaria, 5000 Córdoba, Argentina

ARTICLE INFO

Article history:
Received 9 June 2014
Received in revised form 3 November 2014
Accepted 16 November 2014
Available online 27 December 2014

Keywords:
CoFe films
Electrodeposition
Nanostructured layers
Soft ferromagnetism
Nucleation
Growth mechanisms

ABSTRACT

Co–Fe films are grown onto plane pre-treated Cu foils; the effects of the alloy composition on the morphology and the crystal texture of the electrodeposited films and their anisotropic magnetic hysteresis properties are explored. Nucleation and crystallization mechanisms in these Co-rich layers are also investigated with pulse-reverse plating techniques, using the first cathodic pulse current–time transients. In the diffusion controlled regime the deposition mechanism is found to involve progressive nucleation with three-dimensional (3D) growth, except for the equiatomic $Fe_{50}Co_{50}$ solution where nucleation tends to become instantaneous. The different morphologies and size scales observed are described and correlated with coercivity. The films are electrodeposited onto electrochemically pre-treated Cu substrates from feeds of nominal Fe/Co mol ratios between 0/100 and 50/50. The composition of the deposited layers, as determined by energy dispersive X-ray spectroscopy, are quite close to the nominal values. Cyclic voltammetry determinations exhibit only a single reduction process on the cathode, indicating that a unique ($Co_{100-x}Fe_x$) phase grows. Depending on composition and on the substrate pre-treatment, these layers exhibit textures with features of different sizes. X ray diffraction patterns indicate that the nanostructures with Fe contents above 20 at.% crystallize in a body-centered cubic cell, while samples with Fe contents below this value are *fcc*. Regarding the effect of composition on the morphology, Co and Co-rich layers are compact, with large (100–300 nm) agglomerates of quite equiaxed, densely packed particles (average 50 nm); as the iron content increases above 15 at.%, faceted particles 100 nm in size are observed. All the electrodeposited layers are soft ferromagnetic at room temperature, with an in plane easy axis; coercive fields/forces between 10 mT and 71 mT are measured at 300 K.

1. Introduction

Co–Fe alloys are important soft magnetic materials due to their unique magnetic properties including high saturation magnetization and magnetostriction, high permeability, low coercivity, and a good thermal stability, parameters that cannot be matched by any other alloy system [1]. Their potential applications on miniaturized products, weapons, coatings, communication devices, and for printed circuit boards, among other applications [2–4] make this alloy of industrial importance.

There is today an increasing interest in the development of nanostructured materials because of the unusual physicochemical properties arising from surface as well as quantum effects [5]. Soft and hard magnetic films may be fabricated using sputtering, evaporation and molecular beam epitaxy (MBE) techniques but the low deposition rate, the high vacuum required and the high costs make them unpractical for device fabrication. Sputtering, exhibiting the highest merit, is not suitable, however, for fabricating the thick films demanded by many applications. On the contrary, electrodeposition is one of the simplest, most cheap processes available for the fabrication of single component and multilayered thick (about 10 μm) films.

Chemical and electrochemical methods have been reported to prepare magnetic nanostructures and specially micrometric films; in fact, nanostructures and films of Fe, Ni and Co [6–10] and also CoFe [11–15] films have been successfully produced by these techniques.

In this article we present our results related to the synthesis, using template free electrochemical techniques, of CoFe thick (~10 μm) films with different compositions, onto plane Cu substrates. In the first part, the effect of the substrate surface condition on the morphology and the size scale of the nanostructures deposited is examined for compositions near the 50/50 equiatomic one. In the second part, the effect of the alloy composition on the properties of these structures is addressed. The resulting nanostructure

* Corresponding author. Tel.: +54 0351 433 4051; fax: +54 0351 433 4054.
E-mail address: carmenaguirre@famaf.unc.edu.ar (M. del C. Aguirre).

http://dx.doi.org/10.1016/j.jallcom.2014.11.197
0925-8388/

morphologies and sizes, the crystalline phases present and the room temperature magnetic properties are also described. Finally, the mechanisms operating during this template-free electrodeposition process are briefly commented to identify the main parameters controlling the film growth.

2. Experimental procedures

Thin Cu foils 0.2 mm thick were used as plain substrates. The effect of the substrate surface condition on the final film nanostructure (series I) was investigated for the equiatomic 50/50 nominal composition; in this case the substrates were electrochemically (EC) treated following different procedures, previous to the common metal electrodeposition procedure.

All the chemicals used were of analytical grade: H_3PO_4 (85%) p.a, HNO_3 (65%) p.a, H_2SO_4 (98%) p.a, NaOH (99.9%) p.a, (Cicarelli.). Copper foil 0.2 mm (99.9%) (Alfa Aesar), $FeSO_4.7H_2O \geqslant 99\%$ (Sigma–Aldrich) and $CoCl_2–6H_2O \geqslant 98\%$ (Sigma–Aldrich).They were used in the as received condition, without any further purification.

The initial electrochemical polish was performed in a H_3PO_4 80 wt% solution, at different current densities of 80 and 100 mA/cm^2 for 5 min (EC-80) to (EC-100). In addition to these substrate treatments, a copper foil was first chemically treated in a mixture of (HNO_3/H_3PO_4/Acetic acid, 50/25/25 v/v) and then electrochemically polished in H_3PO_4 80 wt% solution at 100 mA/cm^2 for 5 min (CEC-100). All the foils were then anodized by 10 min in NaOH 0.1 M at a current density of 40 mA/cm^2 and then cathodized by 2 min, to prepare the surface for the metal nucleation during electrodeposition.

The effect of composition on the film nanostructure and morphology was investigated (series II) using copper foils treated in a H_3PO_4 80 wt% solution too, but in this case at a constant potential of 1.5 V, during 5 min (EC-V5). This last potential was selected after cyclic voltammetry experiments because it reproduced the substrate condition of the CEC-100 pre-treatment without a massive copper dissolution during electropolishing; this choice guarantees that any change in the final electrodeposit morphology is due to a different composition. These foils were also anodized by 10 min in NaOH 0.1 M at a current density of 40 mA/cm^2 and then cathodized by 2 min before electrodeposition.

Electrochemical deposition of Co–Fe, was made in a Potentiostat/Galvanostat Autolab302N, under an inert atmosphere. The reference electrode was Ag/AgCl (3 M KCl), the working electrode was an anodized/cathodized copper foil while carbon was used as the counter electrode. First, nominal equiatomic $Co_{50}Fe_{50}$ alloys were fabricated from $CoCl_2$ 0.1 M and $FeSO_4$ 0.1 M solutions at pH 2, using the pulse- and reverse plating potential (PRP), with a starting step of −1.2 V/7.5 s, and then 100 cycles given by −0.3V/1.2 s to −1.2 V/14 s. A nominal $Co_{50}Fe_{50}$ film was also deposited onto a EC-100 substrate by cyclic voltammetry (CV), 60 cycles between −0.3 V and −1.35 V, at a scan rate of 50 mV/s. All these procedures were carried out at room temperature, under a nitrogen atmosphere.

The effect of the alloy composition on the film morphology and nanostructure size and details was investigated in a group of samples (series II), all grown onto substrates electropolished at 1.5 V (EC-V5), from $CoCl_2$ 0.1 M and $FeSO_4$ 0.1 M solutions at pH 2 in different mol ratios, following similar pulse- and reverse plating potential (PRP) procedures, as used for alloys of series I. Samples are named as $Co_{100-x}Fe_x$ where x is the actual at.% Fe concentration.

The resulting structures were characterized by X-ray diffraction (XRD), measured in a Philips PW 3830 diffractometer using Cu Kα radiation (λ = 1.5418 Å), in the 2θ range from 30° to 90°, in the Bragg–Brentano configuration. Sample compositions were determined by energy-dispersive X-ray spectroscopy (EDS), in a JEOL JXA-8230 equipment, while the film morphology was analyzed in a scanning electron microscope (FE-SEM) Zeiss.

The room temperature magnetization vs. field curves were measured in a vibrating sample magnetometer (VSM) Lakeshore 7300, with a maximum field up to 1.5 T; the external field was applied parallel (PA) and perpendicular (PE) to Cu substrate plane.

3. Results and discussion

3.1. Microstructures

3.1.1. $Co_{50}Fe_{50}$ films

The copper substrate pre-treatments largely reduced the surface irregularities, which were the smallest in size for the potentiostatic method at 1.5 V and for the galvanostatic one, at the highest current value of 100 mA cm^{-2}. All the treated substrates revealed the grain structure of the copper foil, allowing an estimation of a mean grain size of about 25 ± 5 μm.

The electrodeposition conditions were selected after investigating the mechanisms involved in the structure development from a solution of nominal composition $Co_{50}Fe_{50}$. Fig. 1 shows the cyclic voltammetry profile, registered during building the sample $Fe_{50}Co_{50}$ in the range between −0.3 to −1.3 V, at a scan rate of 50 mV/s. The cathodic deposition begins at −0.6 V and the nucleation stage extends from this potential, with a wave nucleation potential at −0.8 V and a cross point at −1.0 V. The reverse cycle with the anodic dissolution process up to −0.3 V, would inhibits the adsorbed $M(OH)^+$ species leaving bare substrate for free metal [15–17]. It is worth noting that even when Fe^{2+} and Co^{2+} have different reduction potentials, there exists only one reduction process on the cathode (−0.8V), indicating that a unique CoFe phase is growing. However, in the range of −0.45 to −0.6 V vs. Ag/AgCl the oxidation of CoFe occurs, with preferential formation of free ions during the dissolution of the hydroxide ions.

The EDS analysis contributed to determine the alloy composition prepared by (PRP) onto EC-100 (Co51Fe49); CEC-100 (Co46Fe54) and EC-80 (Co49Fe43O7.9) treated substrates, respectively. In all these cases the film composition was quite close to that of the electrolyte bath. However, the films grown on the less polished substrates contained oxygen, indicating the oxide/

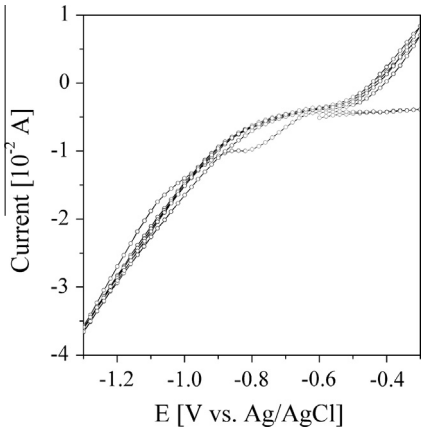

Fig. 1. Three initial cycles during building sample $Co_{54}Fe_{46}$ by cyclic voltammetry between −0.3 V and −1.35 V, at a scan rate of 50 mV/s, showing the anodic dissolution and the nucleation stage in the cathodic section.

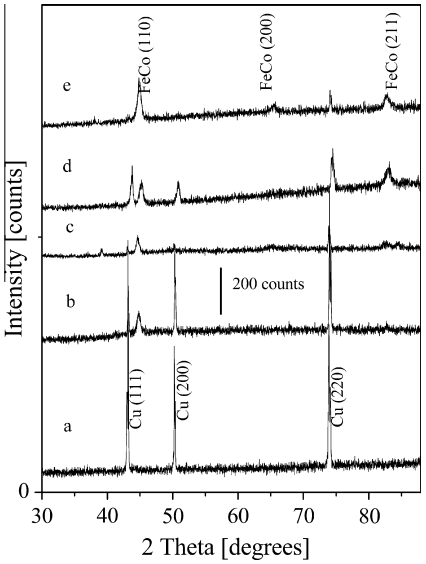

Fig. 2. XRD of samples with compositions near $Co_{50}Fe_{50}$. (a) Copper foil anodized/cathodized; (b) PRP-$Co_{51}Fe_{49}$ (EC-100); (c) CV-$Co_{54}Fe_{46}$ (EC-100); (d) PRP-$Co_{46}Fe_{54}$ (CEC-100) and (e) PRP-$Co_{49}Fe_{43}O_{7.9}$ (EC-80).

Table 1
Chemical (C) and electrochemical (EC) substrate treatments, mean crystallite size d estimated from XRD data, the cell parameter a_0 and the coercive field (force) as measured with the applied magnetic field parallel or perpendicular to the film plane for Fe/Co 50/50 films; the difference $\Delta H=(H_{\perp} - H_{//})$ between the coercivity for applied field parallel and perpendicular to the film plane are also listed.

Sample	Substrate C pre-treatment	Substrate EC treatment	d (nm)	a_0 (A)	$H_{//}$ (mT)	$H_{\perp}$ (mT)	ΔH (mT)
$Co_{49}Fe_{43}O_{7.9}$	–	80 mA/cm^2	23	2.854	19	57	38
$Co_{51}Fe_{49}$	–	100 mA/cm^2	29	2.870	15	41	26
$Co_{54}Fe_{46}$ [†]	–	100 mA/cm^2	23	2.860	24	45	21
$Co_{46}Fe_{54}$	HNO_3/H_3PO_4/Acetic acid, 50/25/25 v/v	100 mA/cm^2	19	2.856	7	28	21

[†] Synthesized by cyclic voltammetry.

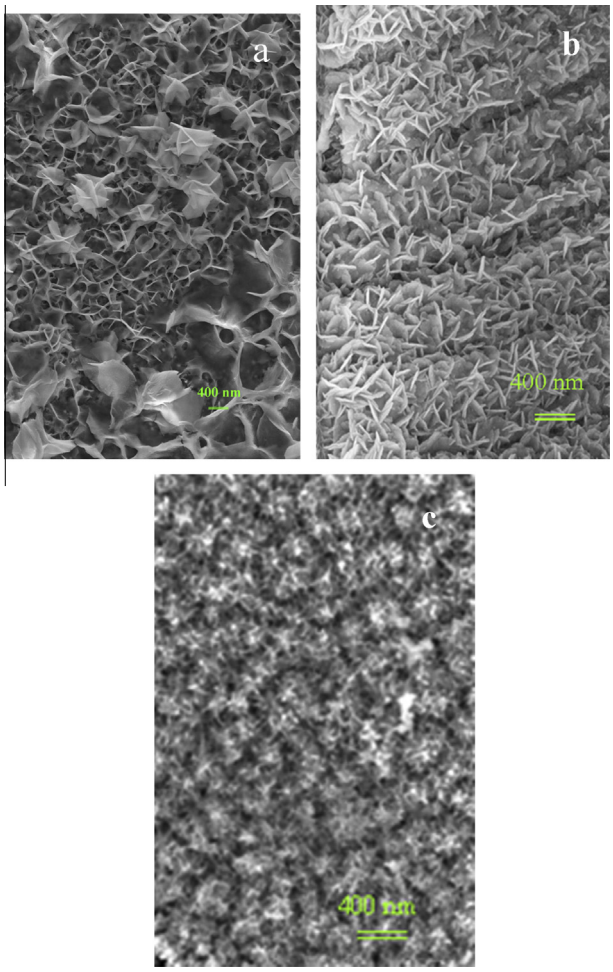

Fig. 3. SEM micrographs (top view) of films with nearly equiatomic compositions; (a) (EC-80)$Co_{49}Fe_{43}O_{7.9}$; (b) (EC-100)$Co_{51}Fe_{49}$ and (c) (CEC-100)$Co_{46}Fe_{54}$.

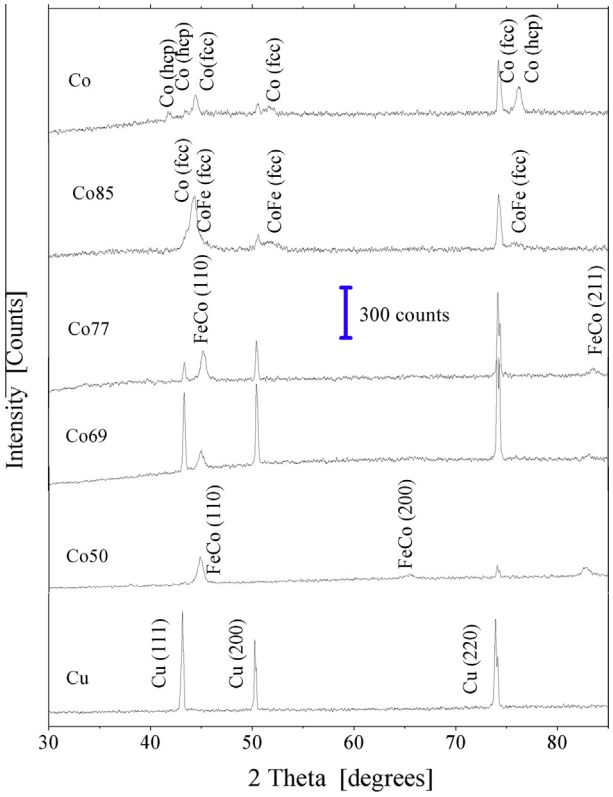

Fig. 4. XRD diffraction patterns of films with nominal compositions $Co_{85}Fe_{15}$, $Co_{77}Fe_{23}$, $Co_{69}Fe_{31}$ and $Co_{50}Fe_{50}$. Those corresponding to the electrodeposited Co film and the Cu substrate foil are also shown for comparison.

hydroxide formation. The X-ray diffraction patterns of nominal $Co_{50}Fe_{50}$ films electrodeposited onto differently pre-treated Cu foils are shown in Fig. 2. The major crystalline phase detected is consistent with the reference pattern of a CoFe *bcc* alloy (JCPDS 00-044-1433). No other phases are evident. From the patterns, the *bcc* cell parameters (a_0) are estimated and from the (1 1 0) peak breath the mean crystallite size (d) is calculated; these two values are included in Table 1.

The film morphology in samples synthesized by pulse and reverse plating potential with nominal composition $Co_{50}Fe_{50}$ is illustrated in Fig. 3. A transition is observed from a microstructure composed by interconnected walls in $Co_{49}Fe_{43}O_{7.9}$ films, with little copper pre-treatment (Fig. 3a), to others containing coarser interconnected walls of about 15 nm thickness and arrays of walls (50–100 nm thick) as in the $Co_{51}Fe_{49}$ alloy, Fig. 3b; in this case the substrate is pre-treated at a higher current density (EC-100) being the electrodeposition conditions identical. Fig. 3c shows the $Co_{46}Fe_{54}$ film deposited onto a copper foil first chemically treated and then electrochemically polished (CEC-100). This film without oxygen exhibits a similar morphology but in a finer scale than the former, indicating that this two step substrate pre-treatment improves the iron incorporation in the alloy, avoids oxidation and reduces the nanostructure scale size. It is expected [11–15] that during the anodic pulse portion $Fe(OH)^+$ and $Co(OH)^+$ dissolve into the plating solution due to the surface metal atoms dissolution. Thus, the anodic dissolution process eliminating the hydroxides and a smooth surface, improving the deposition environment, favor the formation of these CoFe intricate nanostructures.

3.1.2. Effect of the alloy composition in $Co_{100-x}Fe_x$ films

The X-ray diffraction patterns corresponding to the films with different compositions are depicted in Fig. 4, together with those from the pure Co film and the Cu substrate foil. All the deposits are nanocrystalline and the profiles are in good agreement with

Table 2
Mean crystallite size d estimated from XRD data, the cell parameter a_0 and the coercive field (force) as measured with the applied magnetic field parallel or perpendicular to the film plane for different Co/Fe compositions; the differences $\Delta H = (H_{\perp} - H_{//})$ are listed.

Sample	Substrate EC treatment	d (nm)	a_0 (A)	$H_{//}$ (mT)	$H_{\perp}$ (mT)	ΔH (mT)
Co	1.5 V/5′	29	3.354 *fcc*	15	41	26
		23	2.501 *hcp*			
$Co_{85}Fe_{15}$	1.5 V/5′	18	3.534 *fcc*	14	22	8
$Co_{77}Fe_{23}$	1.5 V/5′	23	2.837 *bcc*	11	19	8
$Co_{69}Fe_{31}$	1.5 V/5′	29	2.839 *bcc*	21	71	50

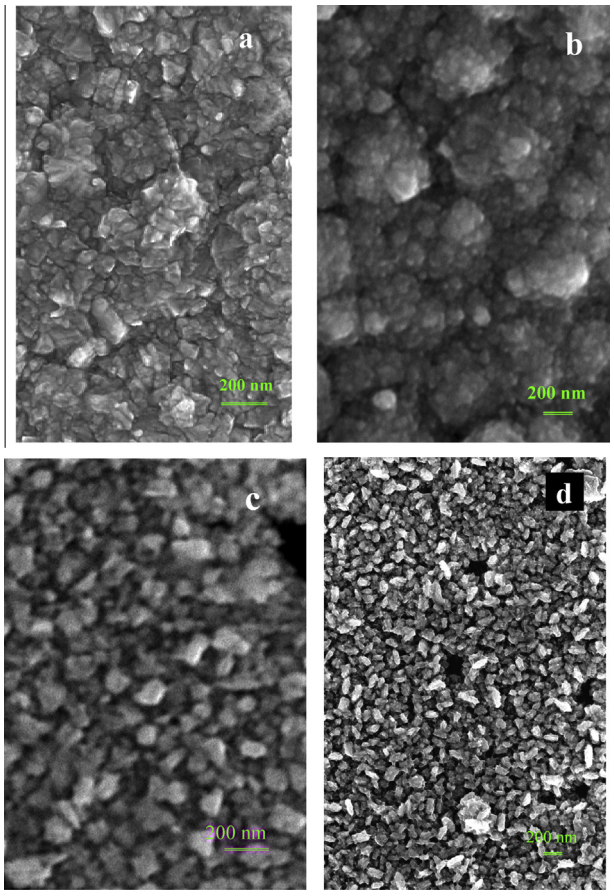

Fig. 5. SEM top view images of (a) Co_{100}; (b) $Co_{85}Fe_{15}$; (c) $Co_{77}Fe_{23}$ and (d) $Co_{69}Fe_{31}$.

reference patterns; the pure Co layer contains both *hcp* (JCPDS 00-001-1278) and *fcc* (JCPDS 00-015-0806) Co grains; for large Co contents the Co(Fe) alloys are *fcc* while they become *bcc* for a concentration of 80 at.% Co or less (CoFe: JCPDS 00-044-1433; $Co_{70}Fe_{30}$: JCPDS 00-048-1818). The maximum intensity at $2\theta = 43.1°$ corresponds to the (1 1 1) main line from the Cu pretreated substrate. As before, a profile fitting was made to the CoFe maxima in each pattern to determine the average crystallite size of the monophase film, using the Scherrer formulae, after correcting for instrumental broadening. The corresponding values, between 18 nm and 30 nm, are listed in Table 2 together with the cell parameters values determined; the cell parameter a_0 in *bcc* Co(Fe) alloys is found to decrease as the Fe content in the sample diminishes.

As pointed out before, the $Co_{100-x}Fe_x$ ($x = 0$, 15, 23, 31) films were electrodeposited onto Cu foils pre-treated at a constant potential of 1.5 V during 5 min. As discussed, this potential was selected after several cyclic voltammetry assays because it reproduced in a nominal $Co_{50}Fe_{50}$ film the fine and uniform microstructure obtained after a pre-treatment CEC-100 (see Fig. 3c); this choice guarantees that any change in morphology is due to a different composition.

Depending on the Fe content the films exhibit different morphologies; the film with a composition Co_{100} is relatively dense and consists of large agglomerates (100–300 nm) of quite equiaxed particles (average 50 nm), as illustrated in Fig. 5a. The mean *hcp* Co crystallite size estimated with the Scherrer equation is about 23 nm. Samples $Co_{85}Fe_{15}$ exhibit a less regular surface – Fig. 5b- with small spheroidal grains, highly agglomerated; it may be observed that new grains form on the top of the old agglomerates, indicating that a nucleation process also takes place during growing. These new crystals are likely to appear by a progressive nucleation mechanism, where new crystalline nucleus continuously form during the electrodeposition process. Fig. 5c and d show samples with composition $Co_{77}Fe_{23}$ and $Co_{69}Fe_{31}$ respectively; these layers with larger iron contents exhibit an irregular morphology, with non agglomerated prismatic grains/particles of about $200 \times 100\ nm^2$ in section; these structures are consistent with a reduced nucleation rate and an enhanced growing rate. As previously discussed, the equiatomic sample – Fig. 3a – exhibits new features; in addition to the uniformly distributed particles (50 nm), thin inter-connected walls and wires grow around some of them, giving to the layer surface a complex texture. From these results it may be concluded that as the Fe content increases the film morphology becomes more intricate.

3.2. Magnetic properties

The room temperature hysteresis loops of as deposited $Co_{50}Fe_{50}$ samples are shown in Fig. 6 and those corresponding to films with different Fe contents are depicted in Fig. 7; for all the synthesis procedures and compositions they are soft ferromagnetic, with relatively high [18] coercive fields/forces between 10 mT and 60 mT. The magnitudes corresponding to each as deposited sample are listed in Table 1. It may be observed that a high coercivity is associated to vertically developed, columnar and/or wall-like grain structures. Coercivity is frequently reported to decrease with the film thickness [18]; in our case, the layers have thickness in the range of (8 ± 2) μm, (see Fig. 8) and no clear correlation with coercivity could be established. Then, coercivity is likely to depend on the film nanostructure.

The different loop shapes observed for magnetic fields applied parallel and perpendicular to the layer plane are consistent with an in plane easy axis and an out of plane hard axis. It is worth to note that in all the samples, the coercive field is slightly larger when the magnetic field is applied perpendicular (PE) to the film plane indicating that the easy and the soft axis were coincident. The difference in the coercive field value measured parallel (PA) and perpendicular (PE) to the Cu substrate is larger in microstructures with particle and/or pillar like morphologies as in $Co_{69}Fe_{31}$. Considering that in these samples the Co content is lower, the relatively high coercivity can be attributed to the sample morphology. In fact, the samples exhibiting both, large coercive fields values and also large differences in coercivity when measured in configurations

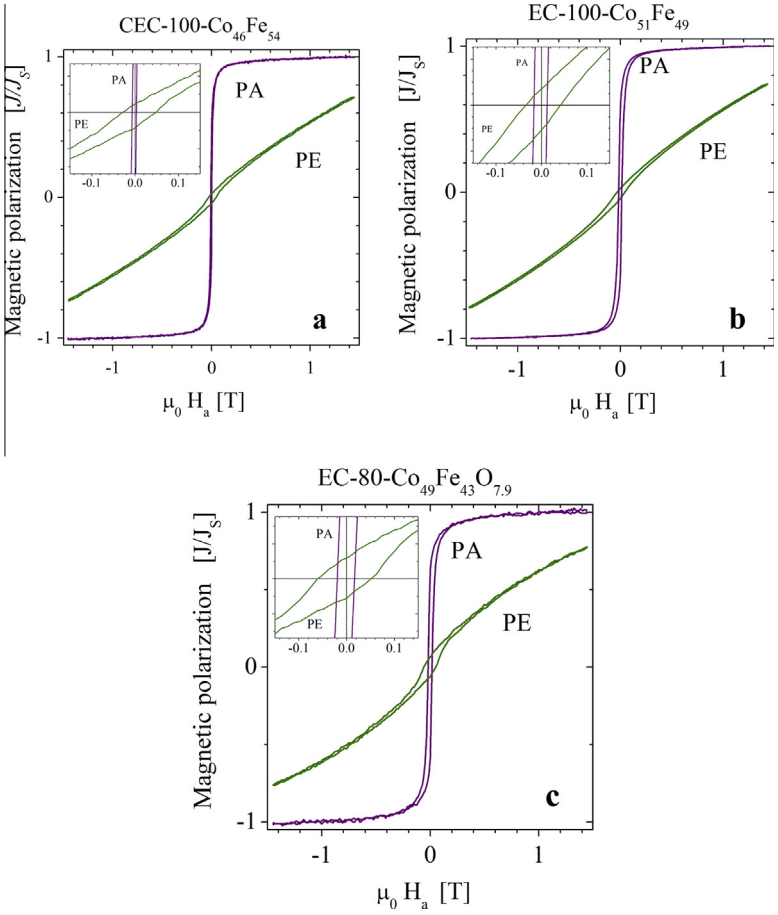

Fig. 6. Room temperature hysteresis loops corresponding to as deposited films with nominal compositions near 50/50, measured in both configurations, with the applied magnetic field parallel (PA) and perpendicular (PE) to the layer plane.

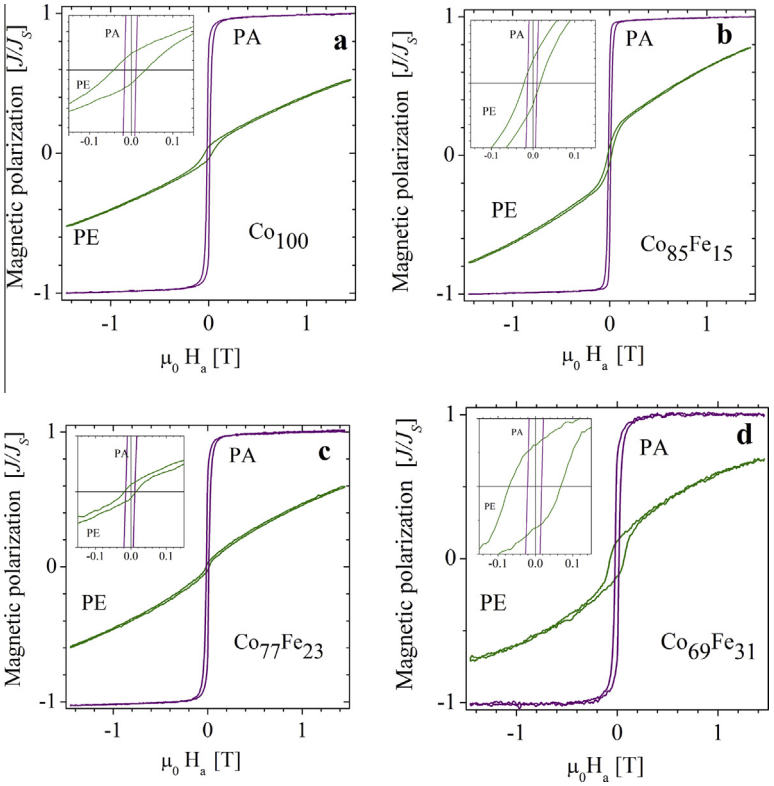

Fig. 7. Room temperature hysteresis loops corresponding to the as deposited CoFe films with different Fe content, measured with the magnetic field parallel (PA) and perpendicular (PE) to the film plane.

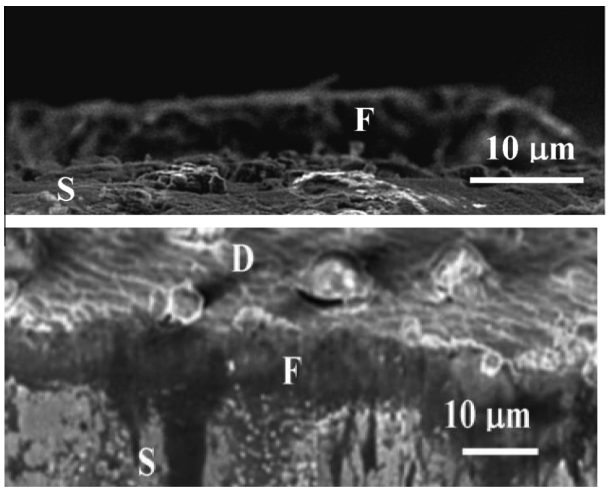

Fig. 8. SEM image of the film F deposited onto a substrate S for samples $Co_{77}Fe_{23}$ (top) and $Co_{69}Fe_{31}$ (bottom). D denotes the upper layer face.

PA and PE are those containing small size, isolated particles or wall-like intricate structures.

Only the films with pure or 85 at.% Co are relatively compact; samples with higher iron contents, having a *bcc* lattice, exhibit complex, more open morphologies involving particles/pillars, thin walls and/or nanowire networks.

3.3. Electrodeposition mechanisms

Samples with the same feed composition ($Fe_{50}Co_{50}$) were also prepared by pulse- and reverse plating potential (PRP). This electrodeposition mode allows to separate and identify the nucleation and the growth mechanisms, operating during electrodeposition onto a plane substrate. Fig. 9 shows the pulse-reverse response currents as functions of time, for all the deposits. Fig. 9a shows the response current for samples with nominal composition $Fe_{50}Co_{50}$; currents between −0.009 A and 0.004 A are measured for samples $Co_{54}Fe_{46}$ and $Co_{51}Fe_{49}$, and between −0.01 A and 0.005 A, in samples $Co_{49}Fe_{41}O_{7.9}$, observing a higher deposition rate in this last case. The results obtained in samples with increasing Co content are shown in Fig. 9b; when the pulse-plating current of samples $Co_{100-x}Fe_x$ are compared, it may be observed that the Co-rich deposits grow at higher deposition rates than the Fe-rich ones; this may be rationalized by considering that the nucleation over potential for depositing Fe is more negative (−0.44 V vs. SHE) than the Co nucleation over potential (−0.27 V vs. SHE). The deposition rate of $Co_{69}Fe_{31}$ and $Co_{77}Fe_{23}$ samples are similar, with the pulse- and reverse –plating currents close to −0.012 A and 0.005 A, respectively; these values are somewhat higher than in $Co_{85}Fe_{15}$ (−0.010 A and 0.004 A). On the other hand, the Co_{100} sample exhibited a current range between −0.008 A and 0.003 A with a slower deposition rate than that for Co-rich alloys, but similar to that observed for the nominal Co50Fe50 composition, most likely by a surface effect on nucleus formation.

Low current densities promote slow electrodeposition rates; at higher current densities, as in Co-rich samples, the electrodeposition rate is higher and the cathodic polarization is favored leading to fine grained, dense coatings.

It has been reported [15–17] that during anodic re-dissolution hydroxilated species ($Co(OH)^+_{ads}$ $Fe(OH)^+_{ads}$) are discarded on surface, whose adsorption mechanism to the surface depends in part on the process rate. In pulse-and reverse plating potential cycles, the anodic dissolution takes place during the step to −0.3 V.

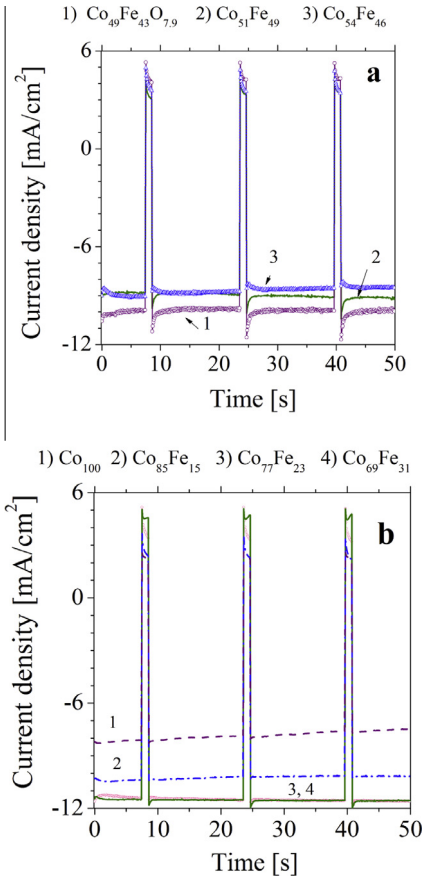

Fig. 9. Current density for potentiostatic pulse-reverse-plating of (a) (EC-80)$Co_{49}Fe_{43}O_{7.9}$ (1); (EC-100)$Co_{51}Fe_{49}$ (2) and (CEC-100)$Co_{54}Fe_{46}$ (3); (b) Co_{100} (1); $Co_{85}Fe_{15}$ (2); $Co_{77}Fe_{23}$ (3) and $Co_{69}Fe_{31}$ (4).

The cathodic pulse at −1.26 V initiates the nucleation process and the first cathodic transient for 7.2 s is used to explore the nucleation and growth behaviors and the operating mechanisms in the different $Co_{100-x}Fe_x$ alloys. Assuming that these nanostructures develop by a nucleation and diffusion controlled growth mechanism, and that not two but only one effective specie of average density ρ_{av} and mean atomic weight M_{av} is involved in the process, a well known diagnostic method [19–21] can be used to determine if nucleation proceeds in 2D or 3D, and if it is instantaneous (I) or progressive (P) in character. The experimental current i vs. time t is first normalized to the maxima current i_m and time t_m values, respectively. Then, dimensionless $\frac{i}{i_m}$ vs. $\frac{t}{t_m}$ curves, based on the theoretical model proposed by Scharifker–Hills [19] for hemispherical nucleus (3D), and on the model proposed by Bewick, Fleischman, Thirsk, (BFT model) [20] for 2D nucleation (both formulated for single pure elements), are plotted together with the experimental normalized data for comparison. These dimensionless theoretical curves are given by:

$$\frac{i}{i_m} = \left(\frac{t_m}{t}\right)\left\{\exp\left[\left(\frac{t^2 - t_m^2}{2t_m^2}\right)\right]\right\} \quad \text{2DI} \tag{1}$$

$$\frac{i}{i_m} = \left(\frac{t}{t_m}\right)^2\left\{\exp\left[\left(\frac{-2(t^3 - t_m^3)}{3t_m^3}\right)\right]\right\} \quad \text{2DP} \tag{2}$$

$$\frac{i}{i_m} = \left(\frac{1.9542t_m}{t}\right)^{1/2}\left\{1 - \exp\left[1.2564\left(\frac{t}{t_m}\right)\right]\right\} \quad \text{3DI} \tag{3}$$

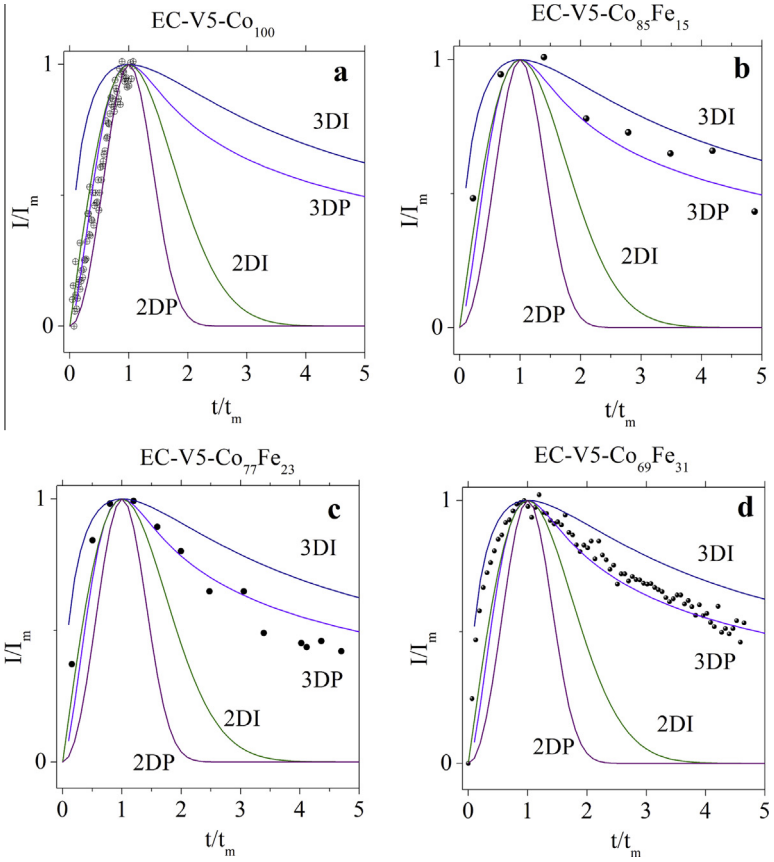

Fig. 10. Non-dimensional plots of (I/I_m) vs. t/t_m (Eqs. (1)–(4)) and the measured values corresponding to samples: (a) Co_{100}, (b) $Co_{85}Fe_{15}$, (c) $Co_{77}Fe_{23}$ and (d) $Co_{69}Fe_{31}$.

$$\frac{i}{i_m} = \left(\frac{1.2254 t_m}{t}\right)^{1/2} \left\{1 - \exp\left[2.3367\left(\frac{t}{t_m}\right)^2\right]\right\} \quad \text{3DP} \tag{4}$$

Figs. 10 and 11 show the theoretical $\left(\frac{i}{i_m}\right)$ vs. $\left(\frac{t}{t_m}\right)$ curves (Eqs. (1)–(4)) plotted together with the experimental data, corresponding to the first cathodic potentiostatic transient in $Co_{100-x}Fe_x$ electrodeposited samples. It may be observed that the curves for Co-rich films (Fig. 10) are consistent with a progressive nucleation model and a 3D diffusion controlled growing mechanism. The Scharifker –Hills [19,21] model can also be applied to calculate the nucleation rate (AN_∞, with A the steady state nucleation rate) and also an effective diffusion coefficient (D_{eff}); from the expressions for 3DP progressive nucleation [19]:

$$i(t) = \frac{zFD_{eff}^{1/2}c}{\pi^{1/2}t^{1/2}}\left\{1 - \exp\left[-\frac{AN_\infty \pi k' D_{eff} t^{1/2}}{2}\right]\right\} \tag{5}$$

with $k' = \frac{4}{3}\left[\frac{8\pi c M_{av}}{\rho_{av}}\right]^{1/2}$ (evaluated in the limit $AN_\infty \; t \to 0$) and $i_m^2 t_m = 0.2598(zFc)^2 D_{eff}$. Then,

$$D_{eff} = \frac{i_m^2 t_m}{0.2598[zFc]^2} \tag{6}$$

with $t_m = \left[\frac{4.6733}{AN_\infty \pi k' D_{app}}\right]^{1/2}$, leading to a progressive nucleation rate of:

$$AN_\infty = \left[\frac{4.6733}{\pi k' D_{eff} t_m^2}\right] \tag{7}$$

Taking the values of $z = 4$, $F = 96{,}500$ C mol^{-1}, $c = 10^{-4}$ mol cm^{-3} and average values of density $\rho_{av} = [(1-x)7.8 + 8.9x]$g cm^{-3} and ionic mass $M_{av} = [(1-x)55.85 + 58.9x]$g mol^{-1}, AN_∞, and D_{eff} are estimated. The resulting values for samples in Fig. 10 are listed in Table 3.

For $Co_{50}Fe_{50}$ nominal samples the agreement between the experimental data and the prediction of the 3D progressive nucleation model becomes poor. As illustrated in Fig. 10, when the Fe content in the bath increases, the first stage of the curve gradually moves from a 3DP regime toward a 3DI one. In the equiatomic samples this deviation is more evident and the data for $t < t_m$ is closer to the 3DI curve, while the second stage with $t > t_m$, seems to preserve a progressive character, at least in CEC-$Co_{46}Fe_{54}$ (for samples EC-$Co_{51}Fe_{49}$ this stage is not available). The resulting values for the two $Fe_{50}Co_{50}$ samples, assuming a 3DP regimen, are displayed in Table 4.

It may be also observed in Table 3 that the effective diffusion coefficient increases with the iron content of the feeding solution, while the nucleation rate decreases. Similar behaviors have been reported for electrodeposition of FeCo films from chloride solutions at pH 2.0 [22], with Fe and Fe-rich depositions fitting an instantaneous nucleation mechanism while Co and Co-rich films evidence a progressive character. Then, increasing the iron content in the solution changes a fast growth of nuclei on many active sites, to a slow growth of nuclei on a smaller number of active sites, all activated during electroreduction. This effect of the iron content may be explained by the changes in the cobalt deposition mechanism imposed by Fe(II) in the solution. In fact, it has been reported [22] that Fe(II) inhibits the nucleation and early growth of Co while the presence of Co(II) strongly catalyzes iron deposition. These phenomena are then at the origin of the different regimes detected and also of the distinct morphologies and size scales observed in the electrodeposited nanostructures as the iron content changes.

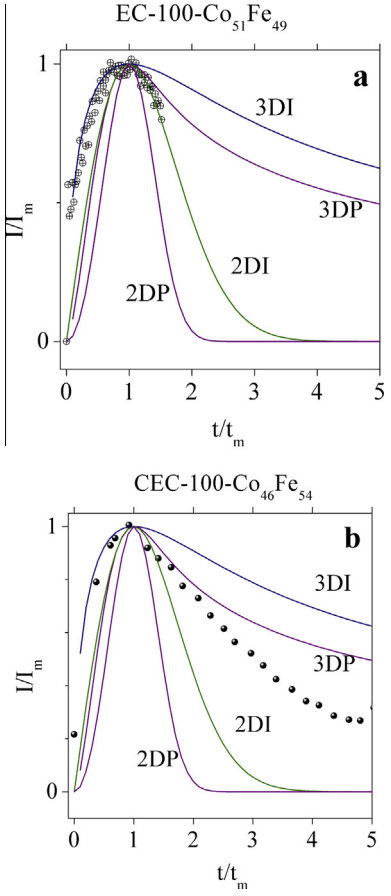

Fig. 11. Non-dimensional plots of (I/I_m) vs. t/t_m (Eqs. (1)–(4)) and the measured values corresponding to samples: (a) (EC-100)$Co_{51}Fe_{49}$ and (b) (CEC-100)$Co_{54}Fe_{46}$.

Table 3
Parameters of the Scharifker–Hills model [Eqs. (5)–(7)] for the Fe/Co samples electrodeposited on a EC treated (5′ at 1.5 V) Cu substrate: the nucleation rate (AN_∞) and the effective diffusion coefficient (D_{eff}) calculated after considering a three dimensional progressive (3DP) nucleation and growth mechanism.

Sample	Substrate EC treatment	$I_m^2\ t_m$ ($A^2\ cm^{-4}\ s$)	k'	D_{eff} (cm^2/s)	AN_∞ ($s^{-1}\ cm^{-2}$)
Co_{100}	1.5 V/5′	13×10^{-3}	0.1719	1.22×10^{-5}	1.20×10^{3}
$Co_{85}Fe_{15}$	15 V/5′	5.8212×10^{-4}	0.1728	0.10×10^{-5}	1.44×10^{8}
$Co_{77}Fe_{23}$	1.5 V/5′	1.1662×10^{-3}	0.1732	0.30×10^{-5}	3.17×10^{7}
$Co_{69}Fe_{31}$	1.5 V/5′	5.7103×10^{-3}	0.1739	1.47×10^{-5}	2.58×10^{5}

Table 4
Parameters of the Scharifker–Hills model [see Eqs. (5)–(7)] for the Fe/Co 50/50 electrodeposited samples: the nucleation rate (AN_∞) and the effective diffusion coefficient (D_{eff}) calculated after considering a three dimensional progressive (3DP) nucleation and growth mechanism.

Sample	Substrate treatment	$I_m^2\ t_m$ ($A^2\ cm^{-4}\ s$)	k'	D_{eff} (cm^2/s)	AN_∞ ($s^{-1}\ cm^{-2}$)
$Co_{51}Fe_{49}$	EC-100	4.316×10^{-3}	0.1748	1.11×10^{-5}	4.56×10^{4}
$Co_{46}Fe_{54}$	CEC-100	2.304×10^{-4}	0.1746	0.06×10^{-5}	8.94×10^{7}

4. Conclusion

$Co_{100-x}Fe_x$ structures have been electrochemically deposited onto flat pre-treated Cu foils, by pulse-and reverse plating potential methods. The resulting Co/Fe molar ratios in the films were close to those in the feed solutions. The chemical and/or electrochemical treatment applied to the substrate before deposition and the iron content were both key parameters determining the film morphology. The pre-treatments given to the substrate only slightly change the morphology of the deposited nanostructures but they largely influence their sizes; the current density affects the deposition rate of the metallic salts and the film growth during the applied pulses.

The samples are polycrystalline, with crystallite sizes between 18 nm and 30 nm. For compositions below 80 at.% Co the layers are *bcc* Fe(Co) alloys while they become Co(Fe) *fcc* structures for larger Co contents; finally for pure cobalt they are a mix of *hcp* and *fcc* cubic phases. All the nanostructures are soft ferromagnetic, with an in plane easy axis; the coercive field values are relatively large, with the out of plane coercivity (19–71 mT) always larger than that measured with the applied field parallel to the film plane (7–24 mT). Samples with high Co content and those with morphologies such as isolated particles/nanopillars or thin interconnected walls exhibit higher coercive fields. In the composition range investigated, most of the depositions are well described by a 3D diffusion controlled growing mechanism, with progressive nucleation; only for the equiatomic $Fe_{50}Co_{50}$ solution, nucleation tends to become instantaneous. The different morphologies observed in $Co_{100-x}Fe_x$ films are the result of the iron content and also of the dissolution process during the anodic pulse.

Acknowledgment

The authors thank to FONCYT-PICT 0074 for financial support.

References

[1] T. Burkert, L. Nordström, O. Eriksson, O. Heinonen, Giant magnetic anisotropy in tetragonal FeCo alloys, Phys. Rev. Lett. 93 (2) (2004). 027203 1–4.
[2] M. Abou-Krisha, F. Assaf, M. Khodari, E. Elkady, Corrosion resistance and electrodeposition behavior of electrodeposited nickel–cobalt–iron alloys, Anti-Corrosion Methods Mater. 59 (4) (2012) 170–177.
[3] M. Coïsson, F. Celegato, P. Tiberto, F. Vinai, Magnetic properties of field-annealed FeCo thin films, J. Magn. Magn. Mater. 320 (2008) e739–e742.
[4] P. Pernod, V. Preobrazhensky, A. Merlen, O. Ducloux, A. Talbi, L. Gimeno, R. Viard, N. Tiercelin, MEMS magneto-mechanical microvalves (MMMS) for aerodynamic active flow control, J. Magn. Magn. Mater. 322 (9) (2010) 1642–1646.
[5] E. Tosatti, S. Prestipino, S. Kostlmeier, A. Dal Corso, F.D. Di Tolla, String tension and stability of magic tip-suspended nanowires, Science 291 (2001) 288–290.
[6] X. Su, H. Zheng, Z. Yang, Y. Zhu, A. Pan, Preparation of nanosized particles of NiFe and FeCo alloy in solution, J. Mater. Sci. 38 (22) (2003) 4581–4585.
[7] G.S. Chaubey, C. Bracena, N. Poudyal, C. Rong, J. Gao, S. Sun, J. Ping Liu, Synthesis and stabilization of FeCo nanoparticles, JACS Commun. 129 (2007) 7214–7215.
[8] A. Saedi, M. Ghorbani, Electrodeposition of Ni–Co–Fe alloy nanowire in modified AAO template, Mater. Chem. Phys. 91 (2005) 417–423.
[9] D.H. Qin, L. Cao, Q.Y. Sun, Y. Huang, H.L. Li, Fine magnetic properties obtained in FeCo alloy nanowire arrays, Chem. Phys. Lett. 358 (2002) 484–488.
[10] S. Talapatra, X. Tang, M. Padi, T. Kim, R. Vajtai, G.V.S. Sastry, M. Shima, S.C. Deevi, P.M. Ajayan, Synthesis and characterization of Cobalt–Nickel alloy nanowires, J. Mater. Sci. 44 (9) (2009) 2271–2275.
[11] Allen Bai, Chi-Chang Hu, Composition controlling of Co–Ni and Fe–Co alloys using pulse-reverse electroplating through means of experimental strategies, Electrochim. Acta 50 (2005) 1335–1345.
[12] Dong Zhou, Mingge Zhou, Minggang Zhu, Xu Yang, Ming Yue, Electrodeposition and magnetic properties of FeCo alloy films, J. Appl. Phys. 111 (2012) 07A319.
[13] I. Tabakovic, J. Gong, S. Riemer, V. Venkatasamy, M. Kief, Stress evolution in Co_xFe_{1-x} ($x = 0.33–0.87$) electrodeposited films, Electrochim. Acta 55 (2010) 9035–9041.
[14] I. Tabakovic, V. Inturi, J. Thurn, M. Kief, Properties of $Ni_{1-x}Fe_x$ ($0.1 < x < 0.9$) and Invar ($x = 0.64$) alloys obtained by electrodeposition, Electrochim. Acta 55 (2010) 6749–6754.
[15] A. Bai, Chi-Chang Hu, Iron–cobalt and iron–cobalt–nickel nanowires deposited by means of cyclic voltammetry and pulse-reverse electroplating, Electrochem. Commun. 5 (2003) 78–82.
[16] A. Bai, Chi-Chang Hu, Cyclic voltammetric deposition of nanostructured iron-group alloys in high-aspect ratios without using templates, Electrochem. Commun. 5 (2003) 619–624.
[17] B. Tury, M. Lakatios-Varsányi, S. Roy, Ni–Co plated by pulse currents, Surf. Coat. Technol. 200 (2006) 6713–6717.
[18] D. Zhou, M. Zhou, M. Zhu, X. Yang, M. Yue, Electrodeposition and magnetic properties of FeCo alloy films, J. Appl. Phys. 111 (2012) 07A319.

[19] B. Scharifker, G. Hills, Theoretical and experimental studies of multiple nucleation, Electrochim. Acta 28 (7) (1983) 879–889.
[20] A. Bewick, M. Fleischmann, H.R. Thirsk, Kinetics of the electrocrystallization of thin films of calomel, Faraday Soc. 58 (1962) 2200–2216.
[21] B.R. Scharifker, Diffusion controlled growth of hemispheres in ordered arrays, J. Electroanal. Chem. 458 (1998) 253–255.
[22] R. Bertazzoli, D. Pletcher, Studies of the mechanism for the electrodeposition of Fe–Co alloys, Electrochim. Acta 38 (5) (1993) 616.